

DMesh: A Differentiable Representation for General Meshes

Sanghyun Son¹, Matheus Gadelha², Yang Zhou², Zexiang Xu²,
Ming C. Lin¹, and Yi Zhou²

¹ University of Maryland, College Park

² Adobe Research

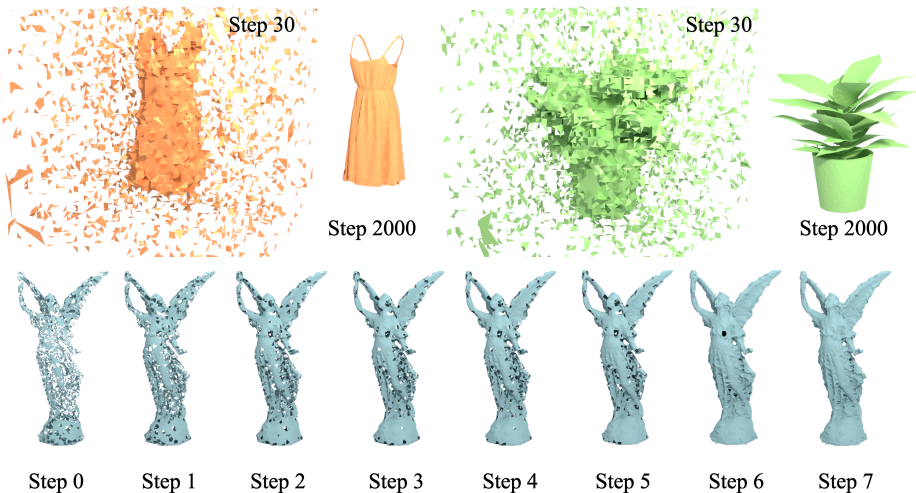


Fig. 1: (→) **Optimization process.** We can start from either random state (up) or initialization based on sample points (down) for faster convergence. Mesh connectivity changes dynamically during the optimization. To make this topology change possible, we compute existence probability for an arbitrary set of faces in a differentiable manner.

Abstract. We present a differentiable representation, **DMesh**, for general 3D triangular meshes. **DMesh** considers both the geometry and connectivity information of a mesh. In our design, we first get a set of convex tetrahedra that compactly tessellate the domain based on *Weighted Delaunay Triangulation* (WDT), and formulate probability of faces to exist on our desired mesh in a differentiable manner based on the WDT. This enables **DMesh** to represent meshes of various topology in a differentiable way, and allows us to reconstruct the mesh under various observations, such as point cloud and multi-view images using gradient-based optimization. The source code and full paper is available at: <https://sonsang.github.io/dmesh-project>³.

Keywords: Differentiable Mesh · 3D reconstruction

³ This paper was last modified at Apr 9, 2024

1 Introduction

Polygonal meshes are widely used in modeling and animation due to their diverse, compact and explicit configuration. Recent AI progress has spurred efforts to integrate mesh generation into machine learning, but challenges like varying topology hinder suitable differentiable mesh representations. This limitation leads to reliance on differentiable intermediates like implicit functions, and subsequent iso-surface extraction for mesh creation [15, 21, 32, 39, 40]. However, meshes generated by such approaches can be unnecessarily dense and misaligned at sharp regions [40], and struggle with open surfaces due to their reliance on the volumetric representation.

The fundamental challenge in creating a differentiable mesh representation lies in formulating both the vertices’ geometric features and their connectivity, defined as edges and faces in a differentiable way. Given a vertex set, predicting their connectivity in a free-form way using existing machine learning data-structures can cost significant amount of computation and be difficult to avoid irregular and intersecting faces. Consequently, most studies on differentiable meshes simplify the task by using a mesh with a *pre-determined* topology and modifying it through various operations [16, 34, 36, 50]. This work, on the contrary, ambitiously aims to establish a general 3D mesh representation, named as DMesh, where both mesh topology and geometric features (e.g. encoded in vertex location) can be simultaneously optimized through gradient-based techniques.

Our core insight is to use differentiable Weighted Delaunay Triangulation (WDT) to divide a convex domain, akin to amber encapsulating a surface mesh, into tetrahedra to form a mesh. To create a mesh with arbitrary topology, we select only a subset of triangular faces from the tetrahedra, termed the “real part”, as our final mesh. The other faces, the “imaginary part”, *support* the real part but are *not* part of the final mesh. We introduce a method to assess the probability of a face being part of the mesh based on weighted points that carry positional and inclusiveness information. Optimization is then focused on the *points’ features*, using a dual power diagram of WDT [3] to generate the triangular mesh. The probability determination allows us to compute geometric losses and rendering losses during gradient-based optimization. This method is essentially a 3D, differentiable extension of \mathcal{A} -shape [29, 30], and a differentiable solution to the problem addressed by constrained Delaunay Triangulation [14, 41, 42].

The key contributions of our work can be summarized as follows.

- We present a novel mesh representation, **DMesh**, which is versatile to accommodate various mesh types for both open surfaces and closed surfaces. The generated meshes are always face-intersection-free.
- We provide efficient reconstruction algorithms for DMesh, which are designed for 3d point cloud and multi-view image inputs. For multi-view reconstruction, we present a differentiable renderer that meets our needs.
- We provide effective regularization methods for DMesh, which can be used for mesh simplification, or triangle quality enhancement.

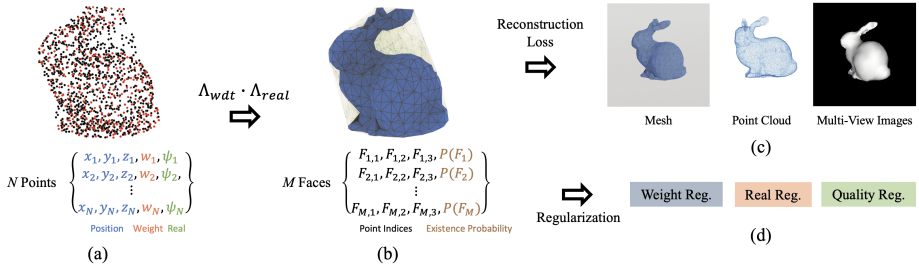


Fig. 2: Our overall framework to optimize mesh according to the given observations. (a): Each point is defined by a 5-dimensional feature vector, which includes position, weight, and real value. Points with larger real values are rendered in red. (b): Given a set of points, we can gather possible faces to exist in our mesh and evaluate their existence probability in differentiable manner. (c): We can compute reconstruction loss by comparing our mesh with given observations, such as mesh, point cloud, or multi-view images. (d): To facilitate the optimization process and enhance the mesh quality, we can use additional regularizations.

- To overcome prohibitively large computational cost of the exact formulation, we propose an efficient relaxation that computes the face existence probabilities with a practical computational cost.

Additionally, to further accelerate the algorithm, we implemented our main algorithm and differentiable renderer in CUDA, which is made available for further research.

2 Related Work

2.1 Shape Representations for Optimization

Neural Implicit Functions The trend of modeling 3D objects as differentiable neural representations has gained popularity in graphics and vision applications, primarily for 3D reconstruction and novel view synthesis, allowing shape optimization through gradient descent and backpropagation [7, 8, 22, 31, 43, 47, 48]. Many methods, inspired by NeRF [31], express scene geometry using volume density and differentiable volume rendering. However, these density-based volumetric approaches don’t always result in accurate 3D geometry. To improve this, several approaches [35, 43, 44, 46] model surface functions as neural signed distance functions (SDFs), converting them to density for rendering and optimization. More recently, neural unsigned distance functions (UDFs) have been developed to model open surfaces, which SDFs can’t describe [24, 25]. While these implicit surface representations show promise in reconstruction, they require iso-surface extraction algorithms like Marching Cubes [26] to convert implicit functions to explicit high-poly meshes, introducing geometric errors. In contrast, our explicit representation can directly output a mesh that can also represent open surfaces, avoiding these issues.

Mesh Representations Previous methods have tried optimizing meshes directly, but often with the assumption of a fixed overall mesh topology [9, 20, 23, 34]. While local connectivity can be altered through remeshing [36], the fundamental geometric topology remains unchanged. Learning-based approaches like BSP-Net [11] allow for topological variation, yet their meshing process isn’t differentiable. Recently, differentiable iso-surface extraction techniques have been developed, resulting in high-quality geometry reconstruction of various topology when combined with Neural or discrete Signed Distance Functions (SDFs) [21, 32, 39, 40, 45]. Some methods even demonstrate backpropagating gradients from mesh vertices to SDF values using non-differentiable techniques like Marching Cubes [28]. However, these surface extraction methods, reliant on SDFs and uniform grids, often need high-poly meshes for accurate reconstruction, regardless of the actual surface’s complexity. Our approach does not have to concern about these issues, because we explicitly define faces and their existence probabilities. See Table 3 for more detailed comparisons to these other methods.

2.2 Shape Representation using Delaunay Triangulation

Delaunay Triangulation (DT) in \mathbb{R}^d connects points whose Voronoi cells share a boundary [3], making it useful for reconstructing shapes from unorganized point sets. It’s been shown that DT of dense samples on a smooth 2D curve includes the curve within its edges [1, 5]. This idea of using DT to approximate shape has been successfully extended to 3D, to reconstruct three-dimensional shapes [2] for point sets that satisfy certain constraints. Our method can be thought of as a differentiable version of these approaches.

Additionally, [38] focused on this DT’s property to connect points and tessellate the domain, and proposed a differentiable WDT algorithm to compute smooth inclusion, or existence score of 2-simplexes (triangles) in 2 dimensional WDT. Our approach develops this approach to compute that score for 2-simplexes in 3 dimensional WDT, which faces different computational challenges than the previous work (Section 3.3). More recently, VoroMesh [27] used similar approach to ours using Voronoi diagram for point cloud reconstruction, but it cannot handle open surfaces and is only confined to point clouds (Section 4).

3 Formulation

In this section, we start with the definition of our new mesh representation. Then we introduce its differentiable formulation, which evaluates the probability of a face to exist in the mesh. Finally we explain how to conquer the computational difficulties posed in our formulation.

3.1 Overall definition

In this work, we take a flexible approach to define a d -dimensional mesh as a set of $(d - 1)$ -simplexes ⁴, and **propose to represent a mesh as a subset**

⁴ They become line segments when $d = 2$, and triangles when $d = 3$.

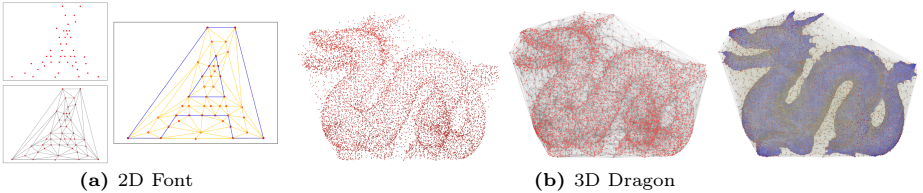


Fig. 3: Illustration of our mesh representation for 2D and 3D cases. **(a):** Our representation in 2D for a letter “A”. **(b):** Our representation in 3D for a dragon model. Blue faces are “*real part*” and yellow ones are “*imaginary part*”.

of WDT. To elaborate, for a given set of d -dimensional points $\mathbb{P} \in \mathbb{R}^d$ and their weights $\mathbb{W} \in \mathbb{R}$, we first obtain the WDT from the weighted points, which tessellates the convex hull of the given points into a compact set of d -simplexes. Then, we extract the desirable $(d - 1)$ -simplexes from the tessellation to define our mesh. Without losing generality, we call the $(d - 1)$ -simplexes as faces here. Among the entire set of faces, we refer the desirable faces as “*real part*”, and the others as “*imaginary part*”. Figure 3 illustrates the cases for $d = 2$ and $d = 3$. Note that the imaginary part is used to sustain the tessellation, even though it is not included in the mesh.

Now let us assume there is a face F that we want to know if it exists in the final mesh or not. Based on the above scheme, we notice that there are two layers of “existence” for F . First, we have to check if F exists in the WDT or not. Formally, we say $F \in \text{WDT}(\mathbb{P}, \mathbb{W})$ if there is a d -simplex in the tessellation induced by WDT that has F as one of its faces. Second, if F exists in WDT, we have to find out if it is included in the “*real part*”. Therefore, we define two predicates, \mathbb{I}_{wdt} and \mathbb{I}_{real} , to evaluate the existence of F in the mesh.

$$\mathbb{I}_{wdt}(F) = \begin{cases} 1 & \text{if } F \in \text{WDT}(\mathbb{P}, \mathbb{W}) \\ 0 & \text{else} \end{cases}$$

$$\mathbb{I}_{real}(F) = \begin{cases} 1 & \text{if } F \in \text{Mesh when } F \in \text{WDT}(\mathbb{P}, \mathbb{W}) \\ 0 & \text{else} \end{cases}$$

Unlike \mathbb{I}_{wdt} , there are various formulations we can use for \mathbb{I}_{real} . In this work, we opt to formulate it using point-wise value $\Psi \in \{0, 1\}$ for the convenience of inference and optimization. When $d = 3$, given a face $F = (p_i, p_j, p_k)$ in $\text{WDT}(\mathbb{P}, \mathbb{W})$, we define $\mathbb{I}_{real}(F)$ as:

$$\mathbb{I}_{real}(F) = \min(\Psi_i, \Psi_j, \Psi_k).$$

Note that all of the three points should have a value of 1 to make F to be considered in the “*real part*”. Finally, we can define the complete face existence function to determine if a face F exists in the final mesh or not as

$$\mathbb{I}(F) = \mathbb{I}_{wdt}(F) \wedge \mathbb{I}_{real}(F).$$

Differentiable Approach To evaluate the existence of a face F in a differentiable manner, we take a probabilistic approach. That is, we define differentiable functions A_{wdt} and A_{real} that evaluate the following probabilities,

$$A_{wdt}(F) = P(F \in WDT(\mathbb{P}, \mathbb{W})) \quad (1)$$

$$A_{real}(F) = P(F \in Mesh \mid F \in WDT(\mathbb{P}, \mathbb{W})), \quad (2)$$

which produce the following function to determine the final probability of F to exist in mesh:

$$\Lambda(F) = P(F \in Mesh) = A_{wdt}(F) \cdot A_{real}(F).$$

Not only this probabilistic interpretation is important to our differentiable formulation, but also to the downstream tasks that we solve (Section 3.4). In the following section, we discuss the details of A_{wdt} and A_{real} .

Point Features Before moving on to the next section, we'd like to point out that the introduced face existence solely depends on the configuration of the weighted points. Thus, our representation features can be defined purely on the point set. In our representation, each point is defined as a $(d + 2)$ -dimensional vector, d of which represents the spatial position, 1 stands for the weight for WDT, and the remaining 1 is used as ψ , which corresponds to the differentiable version of Ψ (Section 3.2). Note that we set the range of weight and ψ to be $[0, 1]$ in all of our experiments. Our overall framework to optimize our mesh according to the given observations based on these point features is shown in Figure 2.

3.2 Probability Functions

A_{wdt} estimates probability of a face F to exist in WDT (Eq. 1). Our formulation leverages the dual structure of WDT, or Power Diagram (PD) to compute it, following [38]. Note that we develop our theoretical reasoning mainly in 2D for ease of understanding, but it can be extended to 3D easily. To avoid confusion, we denote 1-simplex (line segment) and 2-simplex (triangle) as F_2 and F_3 in this section. Please see Appendix 7 for more detailed discussions.

To start with, given a set of points $\mathbb{P} \in \mathbb{R}^2$ and their weights $\mathbb{W} \in \mathbb{R}$, we call Power cell of p_i in the (dual) PD as C_i . In Figure 4(a), we can see points p_1, p_2 , and p_3 and their corresponding C_1, C_2 , and C_3 in PD. In Figure 4(b, d), C_1 is marked with orange lines. Now, we consider a face F_2 , which connects two points p_i and p_j . Then we can construct its dual line L_F in PD as the intersection of two half spaces defined by the two points. In Figure 4, faces and their dual lines are rendered as solid and dotted blue lines, respectively. In Figure 4(b, d), we can observe that F_2 exists if and only if the two Power cells C_i and C_j share a common edge, and it is a subset of L_F , which holds in general.

Based on this observation, we can measure the unsigned minimum distance between L_F and Power cells C_i and C_j , and use it to identify the existence of F_2 . However, note that the distance stays at 0 when F_2 exists, which means that

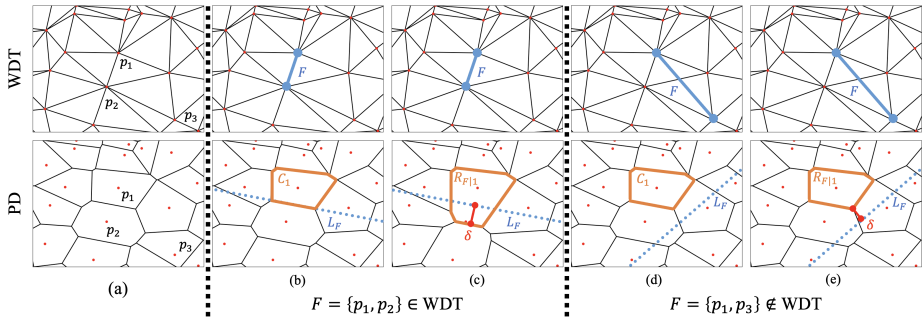


Fig. 4: To compute probability of a $(d-1)$ -simplex F 's existence in WDT (upper row), we investigate its dual PD (lower row). For given F (solid blue), we measure the signed distance δ (red) between its dual L_F (dotted blue) and reduced Power cell (orange) for the estimation. If F exists as shown in (b) and (c), δ becomes positive. In contrast, it evaluates to negative when F does not exist as shown in (d) and (e).

we cannot measure how “stable” F_2 is when it exists. Thus, it is not suitable for measuring differentiable existence probability of F_2 .

To amend this issue, we adopt the concept of reduced Power cell [38]. Reduced Power cell, denoted as $R_{F|i}$, is a Power cell of p_i when ignoring the other point p_j in F_2 . In Figure 4(c, e), we render reduced Power cell $R_{F|1}$ for two different F_2 s in orange lines. Note that when F_2 exists, $R_{F|1}$ gets bigger than C_1 and L_F goes through it, rather than lying on its boundary. When F_2 does not exist, $R_{F|1}$ is just same as C_1 , and thus L_F does not have contact with it.

Now, we newly define a signed distance between L_F and $R_{F|i}$. To that end, we define a signed distance between a random point $P \in \mathbb{R}^2$ and a random reduced Power cell R as follows,

$$\tau_1(P, R) = d(P, R) \cdot (-1)^{1-I(P \in R)},$$

where $d(P, R)$ is the minimum (unsigned) distance between P and R , and $I(\cdot)$ is an indicator function. Then, based on τ_1 , we can define a signed distance between a random line L and R as

$$\tau_2(L, R) = \max_{P \in L} \tau_1(P, R). \quad (3)$$

Observe that the sign of τ_2 is positive when L goes through R , and negative when L does not have contact with R .

Noting that $R_{F|i}$ can exist only when C_i exists⁵, we define the signed distance between the dual line L_F and a reduced Power cell $R_{F|i}$ as

$$\delta(L_F, R_{F|i}) = \begin{cases} \tau_2(L_F, R_{F|i}) & \text{if } \exists C_i \\ -\infty & \text{else} \end{cases} \quad (4)$$

⁵ If the weight of p_i is lower than its neighboring points, there is a chance that C_i does not exist.

Then, the following relationship holds,

$$\delta(L_F, R_{F|i}) > 0 \Leftrightarrow \mathbb{I}_{wdt}(F) = 1.$$

which means, when F exists in WDT, its dual line has positive signed distance to the reduced Power cell of its two ends, and vice versa. Note that this relationship holds for any $x \in \{i, j\}$, because the sign of every $\delta(L_F, R_{F|x})$ is the same. In the right columns of Figure 4(b, c), we can see pink line segments that represent $\delta(L_F, R_{F|1})$.

Then, coming back to $d = 3$, we define a function

$$\Delta(F_3) = \frac{1}{3}(\delta(L_F, R_{F|i}) + \delta(L_F, R_{F|j}) + \delta(L_F, R_{F|k})), \quad (5)$$

which satisfies $\Delta(F_3) > 0 \Leftrightarrow \mathbb{I}_{wdt}(F) = 1$, because the sign of every δ is the same.

Note that this function goes to $-\infty$ if any one of the points in F_3 loses its Power cell. When all of the three points have Power cell, but F_3 does not exist, the function evaluates to a negative value. Finally, it becomes a positive value when F_3 exists. Therefore, we can define a differentiable probability function for the face F_3 to exist in WDT as follows,

$$A_{wdt}(F_3) = \sigma(\alpha_{wdt} \cdot \Delta(F_3)), \quad (6)$$

where σ is a sigmoid function parameterized by α_{wdt} . In our experiments, we set $\alpha_{wdt} = 1000$.

A_{real} evaluates the existence probability of $F_3 = \{p_i, p_j, p_k\}$ in our mesh when it exists in WDT. To define it, we modify per-point discrete value Ψ to ψ , which can have a continuous value in $[0, 1]$. Then, we define A_{real} as,

$$A_{real}(F_3) = dmin(\psi_i, \psi_j, \psi_k, \alpha_{real}),$$

where $dmin$ is a differentiable min operator (Appendix 7), and α_{real} is a hyperparameter for it. We set it as $\alpha_{real} = 100$ in our experiments.

3.3 Computational Difficulties

Although Eq. 4 plays a vital role, it is not trivial to compute it, especially in 3-dimensional space that we are dealing with. For instance, when C_i exists and we have to evaluate Eq. 3, it is not trivial to find an answer to the optimization problem. Moreover, it is hardly possible to compute every reduced Power cell, $R_{F|i,j,k}$, for every possible F_3 .

To overcome these computational difficulties, we propose to leverage lower bound of Eq. 4, which can be efficiently found without constructing any reduced Power cell explicitly. To that end, we treat two cases, $F_3 \in WDT(\mathbb{P})$ and $F_3 \notin WDT(\mathbb{P})$, differently. To be specific, when $F_3 \in WDT(\mathbb{P})$, we define δ_1 as

$$\delta_1(L_F, R_{F|i}) = \tau_1(P_{mid}, R_{F|i}) \geq 0, \quad (7)$$

where P_{mid} is the middle point of the line segment $L_{F|i} = L_F \cap C_i$. The existence of P_{mid} is guaranteed, because L_F is on the boundary of C_i if $F_3 \in WDT(\mathbb{P})$. Note that we can compute Eq. 7 efficiently by projecting P_{mid} to the planes that comprise $R_{F|i}$, because of convexity. This alone reduces a lot of computational burden, because we only have to gather planes that would possibly comprise $R_{F|i}$, instead of explicitly constructing it ⁶. Also, note that δ_1 is a lower bound of δ by definition at Eq. 3.

When $F_3 \notin WDT(\mathbb{P})$, we use following δ_2 :

$$\delta_2(L_F, R_{F|i}) = \tau_2(L_F, C_i) \leq 0. \quad (8)$$

Note that this is lower bound of δ when F_3 does not exist, because C_i is a subset of $R_{F|i}$. Since we can readily obtain C_i from current Power diagram, we can compute minimum distances between L_i and line segments on the boundary of C_i to evaluate Eq. 8.

To sum up, we redefine $\delta(L_F, R_{F|i})$ as follows.

$$\delta(L_F, R_{F|i}) = \begin{cases} \delta_1(L_F, R_{F|i}) & \text{if } \exists F_3 \\ \delta_2(L_F, R_{F|i}) & \text{else if } \exists C_i \wedge \nexists F_3 \\ -\infty & \text{else} \end{cases} \quad (9)$$

Even though this formulation gives a lower bound of Eq. 4, note that when the original function evaluates to 0, this relaxation also evaluates to 0. Therefore, we can still use sigmoid function of Eq. 6 to get differentiable existence probability. Note that in these relaxations, we need to obtain every Power cell C_i , which can be achieved by computing WDT for current point configuration. Please see Appendix 7 and 9 for more details about our formulation, and how it is used in the real optimization process.

3.4 Loss Functions

DMesh could be reconstructed from various types of inputs, such as meshes, point clouds and multi-view images. Given those inputs, we optimize it by minimizing the specific energy functions leveraging the existence probabilities $\Lambda(F)$ of faces F . Here we briefly introduce how we define the reconstruction losses and additional regularization losses that we use in the optimization process. Please see Appendix 8 for more detailed explanations for these loss functions.

Reconstruction Loss (L_{recon}) First, we assume that we are given a ground truth mesh, which is comprised of points \mathbb{P} and faces \mathbb{F} , and we need to represent it with our representation. In this case, we can easily see that we should maximize $\Lambda(\mathbb{F})$, as we already know that they exist in the mesh. In contrast, if we say $\bar{\mathbb{F}}$ as the remaining set of faces that can be defined on \mathbb{P} , we notice that we should

⁶ In our experiments, during optimization process, we keep a set of planes that were on Power cell C_i for each point, and update it during optimization.

minimize $A(\bar{\mathbb{F}})$. Likewise, the reconstruction loss for mesh input can be defined by this explicit connectivity information (Appendix 8.1).

However, when it comes to mesh reconstruction from point clouds or multi-view images, we need to use another form of reconstruction loss. Commonly, we exploit the probabilistic nature of our formulation in defining reconstruction loss for these inputs. For instance, for point cloud, we formulate our loss mainly based on Chamfer Distance (CD) loss, and compute the “expected” CD using our face probabilities (Appendix 8.2). For multi-view images, we define our loss based on rendering loss, which can be computed as L_1 loss between the images of our models rendered by a differentiable renderer and the given images. Here we interpret the face probabilities as face opacities in the rendering process. To allow gradients to flow across the face opacities, we implemented efficient differentiable renderers. Please see Appendix 8.3 for details about them.

Regularizations During optimization, we can employ various regularizations to facilitate the process and enhance the final mesh quality. The first regularization that we introduce is **weight regularization** (L_{weight}), which works on the the dual Power Diagram of WDT (Appendix 8.4). Using this regularization, we intend to reduce the structural complexity of WDT, and discard unnecessary points that are not required to represent our mesh. Note that we can use this regularization because we use WDT, not DT. Using this regularization, we can control the final mesh complexity, as shown in Figure 5.

The next regularization is designed to guide *real* values of points, which is called as **real regularization** (L_{real}). This regularization aims at enforcing nearby points to have similar *real* values. At the same time, it increases *real* values of points that are adjacent to the points of high *real* values (Appendix 8.5). This regularization facilitates the optimization process by removing holes or inner structures of the mesh (Appendix 9), and making the faces near current surface to be considered with higher probabilities than the others.

The final regularization aims at improving the quality of the triangle faces on the mesh, which we name as **quality regularization** (L_{qual}). To be specific, we minimize the average expected aspect ratio of the faces (Appendix 8.6). Using this regularization, we intend to remove thin triangles on the mesh.

Total Loss To sum up, our final loss function can be written as follows:

$$L = L_{recon} + \lambda_{weight} \cdot L_{weight} + \lambda_{real} \cdot L_{real} + \lambda_{qual} \cdot L_{qual},$$

where λ values are hyperparameters. In Appendix 10, we provide values for these hyperparameters for every experiment. Also, in Appendix 10.3, we present ablation studies for these regularizations.

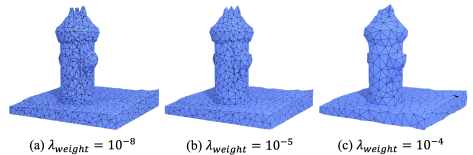


Fig. 5: Results with different λ_{weight} .

4 Experiments and Applications

In this section, we provide experimental results that show the efficacy of our approach. First, when we are given a ground truth mesh, we optimize the point attributes to restore the mesh. With this experiment, we directly prove the differentiability of our design and show the representation power of DMesh. Next, we conduct experiments about 3D reconstruction from point clouds and multi-view images to show how our differentiable formulation can be used in downstream applications. We also show how the regularization affects the reconstruction results through ablation studies.

For the first mesh reconstruction problem, we used three models from Stanford 3D scanning repository [12]. For point cloud and multi-view reconstruction tasks, we used 4 closed-surface models from Thingi32 dataset [49], 4 open-surface models from DeepFashion3D dataset [17], and 3 additional general models that are comprised of both closed and open surfaces from Objaverse dataset [13] and Adobe Stock, to accommodate meshes of various topology. Each of these kinds of models is denoted as “closed”, “open”, and “mixed” model in this section.

We implemented our main algorithm for computing face existence probabilities and differentiable renderer used for multi-view image reconstruction in CUDA [33]. Since we need to compute WDT before running the CUDA algorithm, we used WDT implementation of CGAL [18]. On top of that, we implemented the rest of logic with Pytorch [37]. All of the experiments were run on a system with AMD EPYC 7R32 CPU and Nvidia A10 GPU.

4.1 Mesh to DMesh

In this experiment, we demonstrate that we can preserve most of the faces in the original ordinary mesh after converting it to DMesh using the mesh reconstruction loss introduced in Section 3.4. Please see Appendix 9.1 to learn about the details of the entire optimization process.

In Table 1, we show the recovery ratio (RE) and false positive ratio (FP) of faces in our reconstructed mesh. Note that we could recover over 99% of faces in the original mesh, while only having under 1% of false faces. Please see Appendix 10.1 for more details. This result shows that our differentiable formulation is correct, but also tells us that there is a limitation in converting the original mesh into DMesh using connectivity information. To overcome this limitation, we can reconstruct mesh using other reconstruction losses as discussed in next section. Interestingly, under some occasions, we could observe that our optimized mesh exhibits artificial quad-mesh like pattern (Figure 6),

Table 1: Mesh reconstruction results.

-	Bunny	Dragon	Buddha
RE	99.78%	99.72%	99.64%
FP	0.00%	0.55%	0.84%

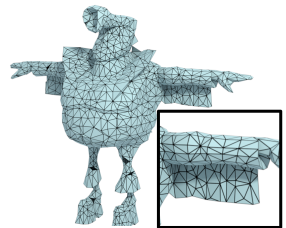


Fig. 6: Reconstruction result that has mesh pattern adaptive to local geometry.

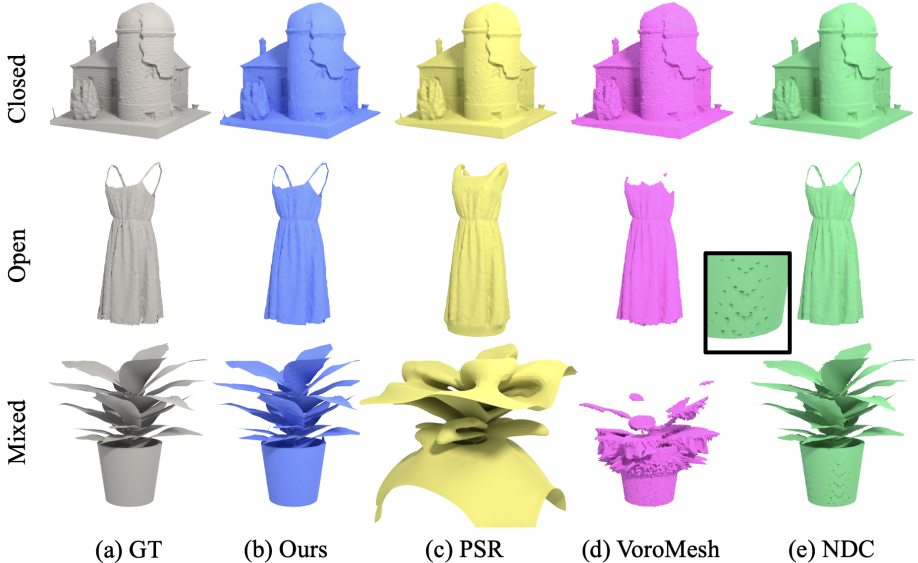


Fig. 7: Point cloud reconstruction results. For a given point cloud sampled from ground truth mesh in (a), our method (b) successfully restores the original shape without losing much detail. In contrast, PSR [19] (c) and VoroMesh [27] (d) fail for open and mixed surface models. NDC [10] (e) exhibits artifacts from grids.

even if we optimize our mesh without ground truth connectivity information, which shows potential ability of our method.

4.2 Point Cloud & Multi-View Reconstruction

In this experiment, we aim to reconstruct a mesh from partial geometric data, such as (oriented) point clouds or multi-view images. For point cloud reconstruction, we sampled 100K points from the ground truth mesh. Even though our formulation can use normal information for better reconstruction (Figure 9), we only use point positions for fair comparison. For

Table 2: Statistics for Point Cloud (PC) and Multi-View (MV) Reconstruction. Best results are highlighted in bold.

	Methods	CD (10^{-3}) ↓			Time (sec) ↓
		Closed	Open	Mixed	
PC	Ours	7.42	6.87	8.06	775.05
	PSR	7.15	26.94	67.18	10.61
	VoroMesh	7.30	26.31	99087.64	12.18
	NDC	7.30	6.83	8.25	3.48
MV	Ours	15.56	11.11	18.33	1434
	Flexicube	31.23	34.91	25.15	56.47
	NIE	31.54	67.37	43.05	6696.43

multi-view reconstruction, we rendered diffuse and depth images of the ground truth mesh from 64 view points. In Appendix 10, we illustrated the example inputs for these experiments. Also, please see Appendix 9 to see the initialization and densification strategy we took in these experiments.

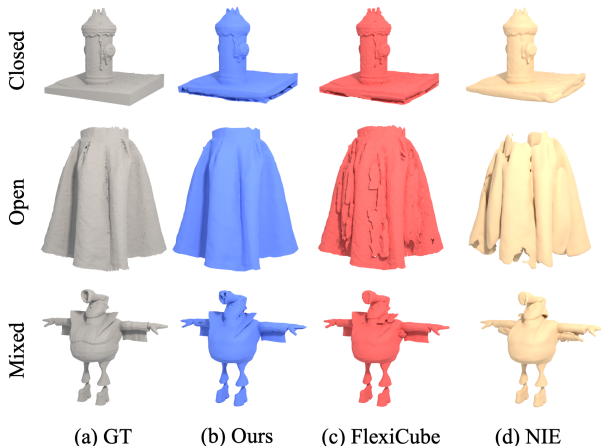


Fig. 8: Multi-view Reconstruction results. For given images captured at multiple viewpoints around the ground truth mesh in (a), our mesh (b) succeeds in reconstructing overall shapes for every model, with small artifacts. However, since (c) FlexiCube [40] and (d) NIE [28] rely on volumetric principles, they produce wrong meshes for open and mixed mesh models.

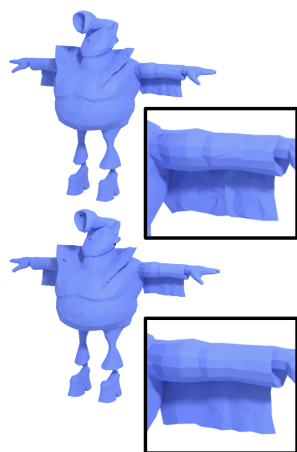


Fig. 9: Point cloud reconstruction results from oriented points. (Up) Reconstruction with $\lambda_{normal} = 0.001$ (Down) Reconstruction with $\lambda_{normal} = 0.01$.

To validate our approach, we compare our results with various approaches. When it comes to point cloud reconstruction, we first compare our result with classical Screened Poisson Surface Reconstruction (PSR) method [19]⁷. Then, to compare our method with optimization based approach, we use recent VoroMesh [27] method, which shares similar principles with us. Note that these two methods are essentially volumetric approach, and thus are not tailored for open surfaces. To compare our method also for the open surfaces, we use Neural Dual Contouring (NDC) [10], even though it is learning-based approach. Finally, for multi-view reconstruction task, we compare our results with Flexicube [40] and Neural Implicit Evolution (NIE) [28], which correspond to volumetric approaches that can directly produce mesh of varying geometric topology for given visual inputs.

In Figure 7 and 8, we visualize the reconstruction results along with the ground truth mesh. In general, volumetric approaches like PSR, VoroMesh, and Flexicube, capture fine details better than our methods for closed models. This is mainly because we currently have limitation in the mesh resolution that we can produce with our method. NIE, which is also based on volumetric principles, generates overly smoothed reconstruction results. However, when it comes to open or mixed mesh models, we can observe that these methods fail, usually with false internal structures or self-intersecting faces (Appendix 10.2). Since NDC leverages unsigned information, it can handle these cases without much

⁷ We also feed in point orientations for PSR, which is optional for our method.

problem as ours. However, we can observe step-like visual artifacts coming from its usage of grid in the final output, which requires post-processing.

Table 2 presents quantitative comparisons with other methods. Chamfer Distance (CD) based on L_1 -norm is computed between the reconstructed mesh and the ground truth mesh, along with an average for different types of meshes. Additionally, we report the average running time of each method. In the table, we observe that CD error generally aligns with the visual renderings. Compared to the other methods, our method exhibits generally better, or comparable results across every model for both point cloud and multi-view reconstruction. However, notice that our method has clear limitation in computation time in the current implementation. This is partially because we run too many steps (Appendix 10.2) for the sake of completeness of every model, but many models converge very fast in practice, as shown in Figure 1 when we use sample points for initialization.

5 Conclusion and Future Directions

Our method achieves a more effective and complete representation of meshes of various topology than existing methods, but opens up areas for future research.

- Computational cost: Currently, the resolution of DMesh is largely constrained by computational cost. Even though we succeeded in decreasing computational burden through our theoretical relaxation and CUDA implementation, it costs more than a second to process over 100K vertices, mainly because we run WDT for the entire points at every step (Appendix 9.2).
- Non-manifoldness: As we have claimed so far, DMesh shows much better generalization than the other methods as it does not have any constraints on the mesh connectivity. However, due to this relaxation of constraint, small holes or “ears” in the reconstruction can appear as “non-manifoldness”. They become more evident when there is no strong supervision or appropriate regularization. Multi-view image reconstruction with occlusions is a typical example. It is possible to eliminate them up to some extent by using additional measures (Appendix 9.2). But, more structured mechanism to eliminate them completely and generate geometric entities that align with more formal definition of “mesh” [4] would be a natural extension.

To address the aforementioned limitations, it is possible to accelerate the main algorithm by carefully constraining the points to update or imposing some bounds on the step size to minimize costly WDT at every iteration. Also, we can investigate if GPU acceleration is possible for WDT [6]. Next, additional geometric constraints can be imposed to remove non-manifold edges. Adopting regularizations like Eikonal loss could be one possible approach, as we can encode unsigned distance information in the points.

Further research can also extend this work to solve other challenging problems (e.g. 3D reconstruction from real world images) or other related applications (e.g. 3D mesh generative model) in the future.

Acknowledgements We thank Zhiqin Chen and Matthew Fisher for helpful advice. This research is a joint collaboration between Adobe and University of Maryland at College Park. This work has been supported in part by Adobe, IARPA, UMD-ARL Cooperate Agreement, and Dr. Barry Mersky and Capital One Endowed E-Nnovate Professorships.

References

1. Amenta, N., Bern, M., Eppstein, D.: The crust and the β -skeleton: Combinatorial curve reconstruction. *Graphical models and image processing* **60**(2), 125–135 (1998)
2. Amenta, N., Bern, M., Kamvyselis, M.: A new voronoi-based surface reconstruction algorithm. In: *Proceedings of the 25th annual conference on Computer graphics and interactive techniques*. pp. 415–421 (1998)
3. Aurenhammer, F., Klein, R., Lee, D.T.: *Voronoi diagrams and Delaunay triangulations*. World Scientific Publishing Company (2013)
4. Botsch, M., Kobbelt, L., Pauly, M., Alliez, P., Lévy, B.: *Polygon mesh processing*. CRC press (2010)
5. Brandt, J.W., Algazi, V.R.: Continuous skeleton computation by voronoi diagram. *CVGIP: Image understanding* **55**(3), 329–338 (1992)
6. Cao, T.T., Nanjappa, A., Gao, M., Tan, T.S.: A gpu accelerated algorithm for 3d delaunay triangulation. In: *Proceedings of the 18th meeting of the ACM SIGGRAPH Symposium on Interactive 3D Graphics and Games*. pp. 47–54 (2014)
7. Chen, A., Xu, Z., Geiger, A., Yu, J., Su, H.: Tensorf: Tensorial radiance fields. In: *European Conference on Computer Vision (ECCV)* (2022)
8. Chen, A., Xu, Z., Wei, X., Tang, S., Su, H., Geiger, A.: Dictionary fields: Learning a neural basis decomposition. *ACM Trans. Graph.* (2023)
9. Chen, W., Ling, H., Gao, J., Smith, E., Lehtinen, J., Jacobson, A., Fidler, S.: Learning to predict 3d objects with an interpolation-based differentiable renderer. *Advances in neural information processing systems* **32** (2019)
10. Chen, Z., Tagliasacchi, A., Funkhouser, T., Zhang, H.: Neural dual contouring. *ACM Transactions on Graphics (TOG)* **41**(4), 1–13 (2022)
11. Chen, Z., Tagliasacchi, A., Zhang, H.: Bsp-net: Generating compact meshes via binary space partitioning. In: *Proceedings of the IEEE/CVF Conference on Computer Vision and Pattern Recognition*. pp. 45–54 (2020)
12. Curless, B., Levoy, M.: A volumetric method for building complex models from range images. In: *Proceedings of the 23rd annual conference on Computer graphics and interactive techniques*. pp. 303–312 (1996)
13. Deitke, M., Schwenk, D., Salvador, J., Weihs, L., Michel, O., Vanderbilt, E., Schmidt, L., Ehsani, K., Kembhavi, A., Farhadi, A.: Objaverse: A universe of annotated 3d objects. In: *Proceedings of the IEEE/CVF Conference on Computer Vision and Pattern Recognition*. pp. 13142–13153 (2023)
14. Diazzi, L., Panozzo, D., Vaxman, A., Attene, M.: Constrained delaunay tetrahedrization: A robust and practical approach. *ACM Transactions on Graphics (TOG)* **42**(6), 1–15 (2023)
15. Guillard, B., Remelli, E., Lukoianov, A., Richter, S.R., Bagautdinov, T., Baque, P., Fua, P.: Deepmesh: Differentiable iso-surface extraction. *arXiv preprint arXiv:2106.11795* (2021)

16. Hanocka, R., Hertz, A., Fish, N., Giryas, R., Fleishman, S., Cohen-Or, D.: Meshcnn: a network with an edge. *ACM Transactions on Graphics (ToG)* **38**(4), 1–12 (2019)
17. Heming, Z., Yu, C., Hang, J., Weikai, C., Dong, D., Zhangye, W., Shuguang, C., Xiaoguang, H.: Deep fashion3d: A dataset and benchmark for 3d garment reconstruction from single images. In: *Computer Vision – ECCV 2020*. pp. 512–530. Springer International Publishing (2020)
18. Jamin, C., Pion, S., Teillaud, M.: 3D triangulations. In: *CGAL User and Reference Manual*. CGAL Editorial Board, 5.6 edn. (2023), <https://doc.cgal.org/5.6/Manual/packages.html#PkgTriangulation3>
19. Kazhdan, M., Hoppe, H.: Screened poisson surface reconstruction. *ACM Transactions on Graphics (ToG)* **32**(3), 1–13 (2013)
20. Laine, S., Hellsten, J., Karras, T., Seol, Y., Lehtinen, J., Aila, T.: Modular primitives for high-performance differentiable rendering. *ACM Transactions on Graphics (TOG)* **39**(6), 1–14 (2020)
21. Liao, Y., Donne, S., Geiger, A.: Deep marching cubes: Learning explicit surface representations. In: *Proceedings of the IEEE Conference on Computer Vision and Pattern Recognition*. pp. 2916–2925 (2018)
22. Liu, L., Gu, J., Lin, K.Z., Chua, T.S., Theobalt, C.: Neural sparse voxel fields. *NeurIPS* (2020)
23. Liu, S., Li, T., Chen, W., Li, H.: Soft rasterizer: A differentiable renderer for image-based 3d reasoning. In: *Proceedings of the IEEE/CVF International Conference on Computer Vision*. pp. 7708–7717 (2019)
24. Liu, Y.T., Wang, L., Yang, J., Chen, W., Meng, X., Yang, B., Gao, L.: Neudf: Leaning neural unsigned distance fields with volume rendering. In: *Proceedings of the IEEE/CVF Conference on Computer Vision and Pattern Recognition*. pp. 237–247 (2023)
25. Long, X., Lin, C., Liu, L., Liu, Y., Wang, P., Theobalt, C., Komura, T., Wang, W.: Neuraludf: Learning unsigned distance fields for multi-view reconstruction of surfaces with arbitrary topologies. In: *Proceedings of the IEEE/CVF Conference on Computer Vision and Pattern Recognition*. pp. 20834–20843 (2023)
26. Lorensen, W.E., Cline, H.E.: Marching cubes: A high resolution 3d surface construction algorithm. In: *Seminal graphics: pioneering efforts that shaped the field*, pp. 347–353 (1998)
27. Maruani, N., Klovov, R., Ovsjanikov, M., Alliez, P., Desbrun, M.: Voromesh: Learning watertight surface meshes with voronoi diagrams. In: *Proceedings of the IEEE/CVF International Conference on Computer Vision*. pp. 14565–14574 (2023)
28. Mehta, I., Chandraker, M., Ramamoorthi, R.: A level set theory for neural implicit evolution under explicit flows. In: *European Conference on Computer Vision*. pp. 711–729. Springer (2022)
29. Melkemi, M.: A-shapes of a finite point set. In: *Proceedings of the thirteenth annual symposium on Computational geometry*. pp. 367–369 (1997)
30. Melkemi, M., Djebali, M.: Weighted a-shape: a descriptor of the shape of a point set. *Pattern Recognition* **34**(6), 1159–1170 (2001)
31. Mildenhall, B., Srinivasan, P.P., Tancik, M., Barron, J.T., Ramamoorthi, R., Ng, R.: Nerf: Representing scenes as neural radiance fields for view synthesis. *Communications of the ACM* **65**(1), 99–106 (2021)
32. Munkberg, J., Hasselgren, J., Shen, T., Gao, J., Chen, W., Evans, A., Müller, T., Fidler, S.: Extracting triangular 3d models, materials, and lighting from images. In: *Proceedings of the IEEE/CVF Conference on Computer Vision and Pattern Recognition*. pp. 8280–8290 (2022)

33. Nickolls, J., Buck, I., Garland, M., Skadron, K.: Scalable parallel programming with cuda: Is cuda the parallel programming model that application developers have been waiting for? *Queue* **6**(2), 40–53 (2008)
34. Nicolet, B., Jacobson, A., Jakob, W.: Large steps in inverse rendering of geometry. *ACM Transactions on Graphics (TOG)* **40**(6), 1–13 (2021)
35. Oechsle, M., Peng, S., Geiger, A.: Unisurf: Unifying neural implicit surfaces and radiance fields for multi-view reconstruction. In: *International Conference on Computer Vision (ICCV)* (2021)
36. Palfinger, W.: Continuous remeshing for inverse rendering. *Computer Animation and Virtual Worlds* **33**(5), e2101 (2022)
37. Paszke, A., Gross, S., Chintala, S., Chanan, G., Yang, E., DeVito, Z., Lin, Z., Desmaison, A., Antiga, L., Lerer, A.: Automatic differentiation in pytorch (2017)
38. Rakotosaona, M.J., Aigerman, N., Mitra, N.J., Ovsjanikov, M., Guerrero, P.: Differentiable surface triangulation. *ACM Transactions on Graphics (TOG)* **40**(6), 1–13 (2021)
39. Shen, T., Gao, J., Yin, K., Liu, M.Y., Fidler, S.: Deep marching tetrahedra: a hybrid representation for high-resolution 3d shape synthesis. *Advances in Neural Information Processing Systems* **34**, 6087–6101 (2021)
40. Shen, T., Munkberg, J., Hasselgren, J., Yin, K., Wang, Z., Chen, W., Gojcic, Z., Fidler, S., Sharp, N., Gao, J.: Flexible isosurface extraction for gradient-based mesh optimization. *ACM Transactions on Graphics (TOG)* **42**(4), 1–16 (2023)
41. Shewchuk, J.R.: Constrained delaunay tetrahedralizations and provably good boundary recovery. *IMR* **193**, 204 (2002)
42. Si, H.: Constrained delaunay tetrahedral mesh generation and refinement. *Finite elements in Analysis and Design* **46**(1-2), 33–46 (2010)
43. Wang, P., Liu, L., Liu, Y., Theobalt, C., Komura, T., Wang, W.: Neus: Learning neural implicit surfaces by volume rendering for multi-view reconstruction. *arXiv preprint arXiv:2106.10689* (2021)
44. Wang, Y., Han, Q., Habermann, M., Daniilidis, K., Theobalt, C., Liu, L.: Neus2: Fast learning of neural implicit surfaces for multi-view reconstruction. In: *Proceedings of the IEEE/CVF International Conference on Computer Vision (ICCV)* (2023)
45. Wei, X., Xiang, F., Bi, S., Chen, A., Sunkavalli, K., Xu, Z., Su, H.: Neumanifold: Neural watertight manifold reconstruction with efficient and high-quality rendering support. *arXiv preprint arXiv:2305.17134* (2023)
46. Yariv, L., Gu, J., Kasten, Y., Lipman, Y.: Volume rendering of neural implicit surfaces. In: *Thirty-Fifth Conference on Neural Information Processing Systems* (2021)
47. Yariv, L., Kasten, Y., Moran, D., Galun, M., Atzmon, M., Ronen, B., Lipman, Y.: Multiview neural surface reconstruction by disentangling geometry and appearance. *Advances in Neural Information Processing Systems* **33** (2020)
48. Zhang, K., Riegler, G., Snavely, N., Koltun, V.: Nerf++: Analyzing and improving neural radiance fields. *arXiv:2010.07492* (2020)
49. Zhou, Q., Jacobson, A.: Thing10k: A dataset of 10,000 3d-printing models. *arXiv preprint arXiv:1605.04797* (2016)
50. Zhou, Y., Wu, C., Li, Z., Cao, C., Ye, Y., Saragih, J., Li, H., Sheikh, Y.: Fully convolutional mesh autoencoder using efficient spatially varying kernels. *Advances in neural information processing systems* **33**, 9251–9262 (2020)